Materials Research Proceedings **27** (2023) 84-94 https://doi.org/10.21741/9781644902455-11

Improving the performance of a lamb wave sensing array via relaxor ferroelectric single crystal transduction

Matthew J. Schipper[1,a], Jaslyn Gray[1,b], David J. Munk[1,c], Scott D. Moss[1,d*], Nik Rajic[1,e], Cedric Rosalie[1,f], Joel Smithard[1,g], Ben Vien[2,h], Wing K. Chiu[2,I], Crispin Szydzik[3,j] and Arnan Mitchell[3,k]

[1]Defence Science and Technology Group, Platforms Division, Victoria, Australia

[2]Monash University, Dept. Of Mechanical Aerospace Engineering, Victoria, Australia

[3]R.M.I.T University, Micro Nano Research Facility, Victoria, Australia

[a]matthew.schipper@defence.gov.au, [b]jaslyn.gray@defence.gov.au, [c]david.munk@defence.gov.au, [d]scott.moss@defence.gov.au, [e]nikolas.rajic@defence.gov.au, [f]cedric.rosalie1@defence.gov.au, [g]joel.smithard@defence.gov.au, [h]ben.vien@monash.edu, [i]wing.kong.chiu@monash.edu, [j]crispin.szydzik@rmit.edu.au, [k]arnan.mitchell@rmit.edu.au

[*] Corresponding author. Tel.: +61-3-9344-2449; fax: +61-3-9626-7089.

Keywords: Acoustic Emission, Damage Detection, Modal Decomposition, Structural Health Monitoring, Relaxor Ferroelectric Single Crystal

Abstract. This paper reports on the potential use of relaxor ferroelectric single crystal (RFSC) transduction to improve the sensitivity of the thin film multi-element Lamb wave sensor called LAMDA (*linear array for modal decomposition and analysis*). The previously reported LAMDA sensor was created using a high-density multi-element polyvinylidene fluoride (PVDF) electro-polymer sensing array. The electromechanical coupling factor $k = d/\sqrt{\varepsilon^T * s^E}$, which is proportional to the piezoelectric coefficient *d*, is considered important for an ultrasonic receiver such as LAMDA. Comparing the PVDF piezoelectric coefficient $d_{31} \approx$ 14 pC/N with that of a recent RFSC [011] $Pb(Mg_{1/3}Nb_{2/3})O_3$-$Pb(Zr,Ti)O_3$ (or Mn-PMN-PZT) having $d_{32} \approx$ -1100 pC/N, suggests the replacement of the PVDF array with a RFSC array could lead to a significant improvement in the sensitivity of the LAMDA sensor and consequently broaden the scope of its potential application to structural health monitoring. To this end, multiphysics modelling has been performed which indicates a five-fold increase in signal voltage output from a Mn-PMN-PZT based RFSC LAMDA compared with the original PVDF LAMDA. Model predictions for both RFSC LAMDA and PVDF LAMDA sensors will be reported, compared, and discussed.

Introduction

A new sensing approach for detecting acoustic emission (AE) called *linear array for modal decomposition and analysis* or LAMDA was recently reported [1]. LAMDA is capable of determining the AE source location and potentially also the type of damage via modal signature analysis [2, 3]. LAMDA, which builds on earlier work in acoustic-wave-mode separation [4-6], incorporates a flexible multi-element array coupled with a high-bandwidth interrogation device [7]. Each individual element in the array is a longitudinal piezoelectric d_{3y}-mode element, where the most sensitive piezoelectric axis being either y= '1' or '2' direction is approximately aligned with the mechanical disturbance, and '3' is the direction of the generated electric field being normal to the surface to which the LAMDA sensor is applied. The initial LAMDA studies employed a 55 μm thick polyvinylidene fluoride (PVDF) sensor for piezoelectric transduction of

Materials Research Proceedings **27** (2023) 84-94 https://doi.org/10.21741/9781644902455-11

acoustic plate waves generated by an AE event such as mechanical impact [1, 8]. The electrical response produced by a LAMDA sensor (i.e. in response to the acoustic plate waves) can be used to locate and potentially quantify a mechanical impact, including any resulting structural damage [2]. LAMDA is thus a powerful new approach for structural health monitoring [9].

The piezoelectric coefficient of the material used to manufacture the LAMDA sensor plays a key role in determining the magnitude of the resulting electric response [10]. For 'PVDF LAMDA' the important piezoelectric coefficient is $d_{31} \approx 13.6$ pC/N [11]. In comparison, a recently developed piezoelectric material known as relaxor ferroelectric single crystal (RFSC) offers significantly higher piezoelectric coefficients, one such example being [011] $Pb(Mg_{1/3}Mb_{2/3})O_3$-$Pb(Zr,Ti)O_3$ (or 'Mn-PMN-PZT') with $d_{32} \approx -1100$ pC/N [12]. With the PVDF d_{31} being almost 80 times smaller than the RFSC d_{32}, a significant improvement in sensitivity might be expected when using RFSC transduction within the LAMDA sensor (henceforth 'RFSC LAMDA'). Since the LAMDA sensors are electromechanical in nature, the electromechanical coupling factor k is expected to play a defining role in determining its sensitivity [10]. The electromechanical coupling factor is defined as $k = d/\sqrt{\varepsilon^T * s^E}$, where ε^T is the permittivity and s^E is the mechanical compliance [13]. The electromechanical coupling factors important for this work are: (i) $k_{31}^{PVDF} = d_{31}/\sqrt{\varepsilon_{33}^T * s_{11}^E}$ for PVDF LAMDA, and (ii) $k_{32}^{RFSC} = d_{32}/\sqrt{\varepsilon_{33}^T * s_{22}^E}$ for RFSC LAMDA [14].

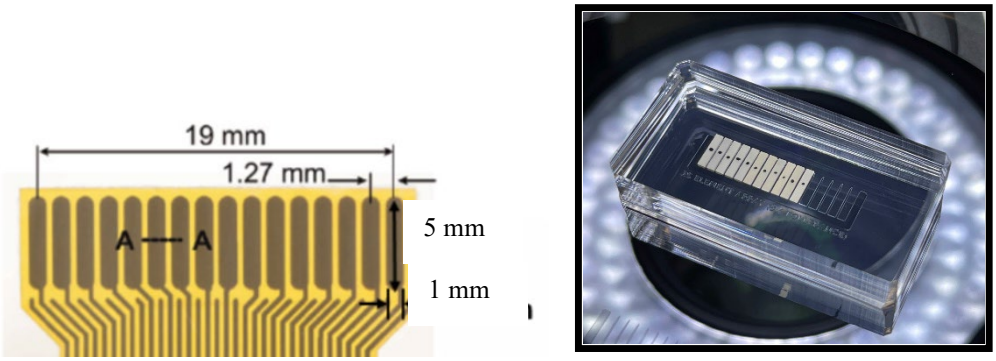

Figure 1. Plan view of 16-element LAMDA sensor (a) PVDF, and (b) RFSC prototype currently being manufactured.

Fig. 1 shows plan view photographs of (a) the existing PVDF LAMDA, and (b) the prototype RFSC LAMDA currently being manufactured. Modelling was performed for both LAMDA sensors shown in Fig. 1 using commercially available software (COMSOL Multiphysics Version 5.6) in order to understand the benefit, if any, that RFSC transduction would provide when compared with the original PVDF approach.

Model details

This section focuses on describing the model geometry used for comparing the PVDF LAMDA and RFSC LAMDA sensors. The modelled geometry comprised a linear array of 16 rectangular piezoelectric elements attached to a circular aluminium plate, 1.6 mm thick with a radius of 70 mm. An infinite element domain was added by extending the radius of the aluminium plate by 5% - this domain minimises the energy of any plate-boundary reflected waves in the model, reducing interference with the modelled piezoelectric response and also shortening the time taken to generate a solution. The elements of the PVDF LAMDA and the RFSC LAMDA sensors were assumed to have identical physical dimensions. As shown in Fig. 1 the individual elements were 1 mm long, 5 mm wide, 55 μm thick, and separated by 0.27 mm. The modelled acoustic impulse source was located at the centre of the aluminium plate, with the nearest LAMDA sensing element

Materials Research Proceedings **27** (2023) 84-94 https://doi.org/10.21741/9781644902455-11

positioned approximately 30.5 mm away. This acoustic source-to-sensor distance was chosen to ensure the sensor was located in the acoustic far-field region, minimising the effects of near-field Lamb wave interference. Each modelled sensing element was electrically grounded at the interface between it and the aluminium plate. The effect of an adhesive bondline between the LAMDA sensor and the aluminium plate was ignored [15].

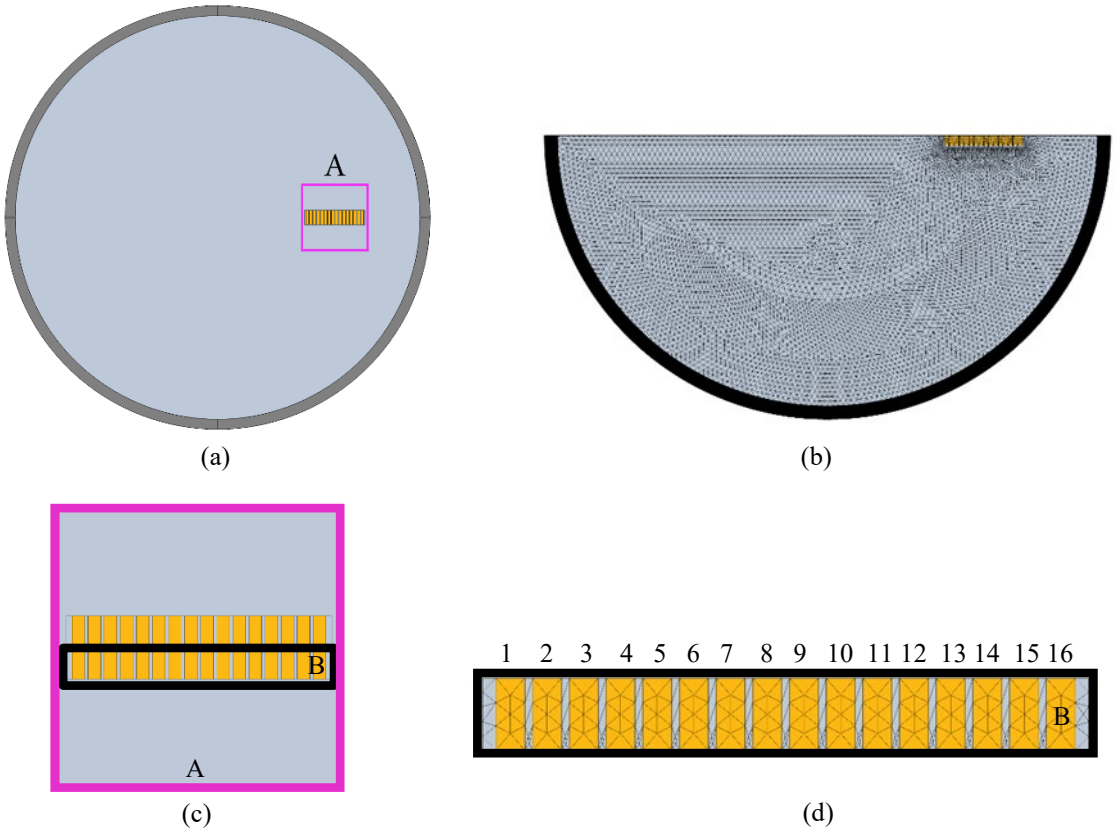

Figure 2. (a) Full model geometry showing the aluminium plate, circumferential infinite element domain, and region 'A' with LAMDA sensor and plate, (b) the model geometry after half-plate symmetric reduction and with model mesh applied, (c) a magnified view of region 'A' containing region 'B' with LAMDA sensor and aluminium plate, and (d) a magnified view of region 'B' with model mesh applied and with the individual elements numbered 1-16. The piezoelectric sensing elements are represented as orange domains, the aluminium is light-grey, and the dark-grey circumferential domain is the infinite element domain.

Fig. 2a is a schematic of the modelled geometry comprising a circular metal plate with a LAMDA mounted in the region designated as 'A'. To reduce the degrees of freedom in the model (and hence reduce the model solve time) the geometry shown in Fig. 2a was split along the horizontal x-axis using a symmetric boundary condition. The lower half of the model depicted in Fig. 2b was used for solving and generating results. Additionally, a box 1.6 mm thick, 21 mm long, 5 mm wide, and centred on the LAMDA sensing element was added to the model. The box was used during the model meshing sequence to increase the mesh density in the region of the LAMDA sensor. Fig. 2b illustrates the resulting half-plate symmetric geometry, and Fig. 2c is a magnified view of region 'A' (magenta outlined square in Fig. 2a). Mapped onto Fig. 2d is the mesh used to model the LAMDA sensor. The material parameters used in the model are listed in Appendix A. Table A1 contains the material properties used to model the aluminium plate, with Tables A2 and A3 providing the electromechanical properties for PVDF and the RFSC Mn-PMN-PZT respectively. The in-plane piezoelectric coefficient for RFSC is largest in the 2-direction (i.e. d_{32}),

whereas for PVDF it is largest in the 1-direction (i.e. d_{31}). The orientation of the piezoelectric material was defined in the model as a rotational system that was pre-defined depending on the material being modelled, with the largest piezoelectric coefficient parallel to the x-axis (horizontal axis in Figs. 2 and 3). Fig. 3 indicates the crystalline orientation of the PVDF and RFSC elements.

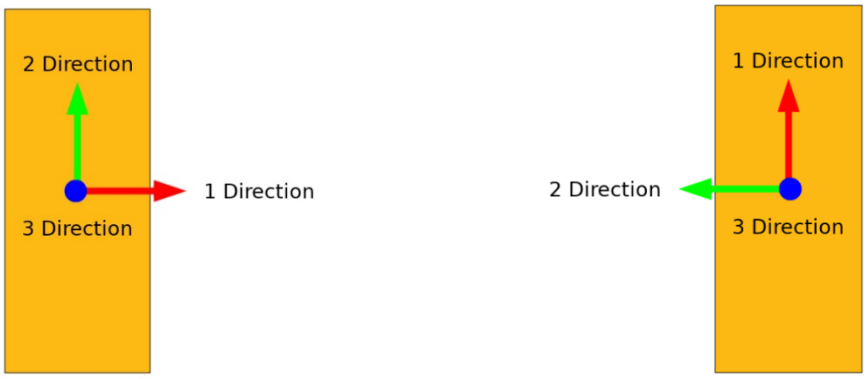

(a) (b)

Figure 3. Crystalline orientation for the individual elements of the (a) PVDF LAMDA and, (b) RFSC LAMDA sensors.

Modelled acoustic impulse

This section focuses on the modelled mechanical impulse used to produce surface acoustic (Lamb) waves in the aluminium plate. The mechanical impulse was applied normal to the centre of the plate as a pair of coupled point forces, located at the top and bottom of the plate centre, that were equal in direction and magnitude [16]. This impulse force selectively generated the asymmetric A0 wave, being the wave-type that produced the largest voltage response in the LAMDA piezoelectric elements. The impulse function used was the Hann-Windowed wave defined in Eq. 1,

$$F(t) = F_0 \sin^2\left\{\frac{\pi f}{C}(t - t_0)\right\} \sin\{2\pi f(t - t_0)\}\ ,\ (t_0 \le t \le L + t_0) \tag{1}$$

where $F(t)$ is the impulse force at time t for a wave of C cycles, F_0 is the impulse amplitude, t_0 is a time delay, and f is the centre frequency (see Appendix B for details). The time delay allows for the inclusion of a quiescent period in the simulation to prevent instantaneous model stresses. In this study a delay of $t_0 =$ 50 nanoseconds was used. The number of cycles chosen was 3.5, and the solver was run for three centre frequencies, 100, 200, and 500 kHz. The amplitude of the impulse force was set to 0.5 N, which due to the halving of the plate geometry corresponds to a 1 N force for the full geometry. Fig. 4a is an example of the applied impulse wave force-time history corresponding to a centre frequency of 500 kHz (and includes the additional $t_0 =$ 50 nanoseconds of delay).

In the present work, for the impulse force described by Eq. 1, the bandwidth was defined as twice the centre frequency to cycle-number ratio,

$$B = 2 \cdot \frac{f}{C}\,, \tag{2}$$

with the equivalent bandwidth indicated by a dotted horizontal line in Fig. 4b for an impulse with a centre frequency of 500 kHz. Eq. 3 was used to find the effective maximum frequency of the impulse,

$$f_{max} \approx f \cdot \left(1 + \frac{2}{C}\right) \tag{3}$$

The effective maximum impulse frequency is important since it was used to define the solver time-step. The black-dashed vertical line Fig. 4b is an example of the maximum frequency used for an impulse with a centre frequency of 500 kHz.

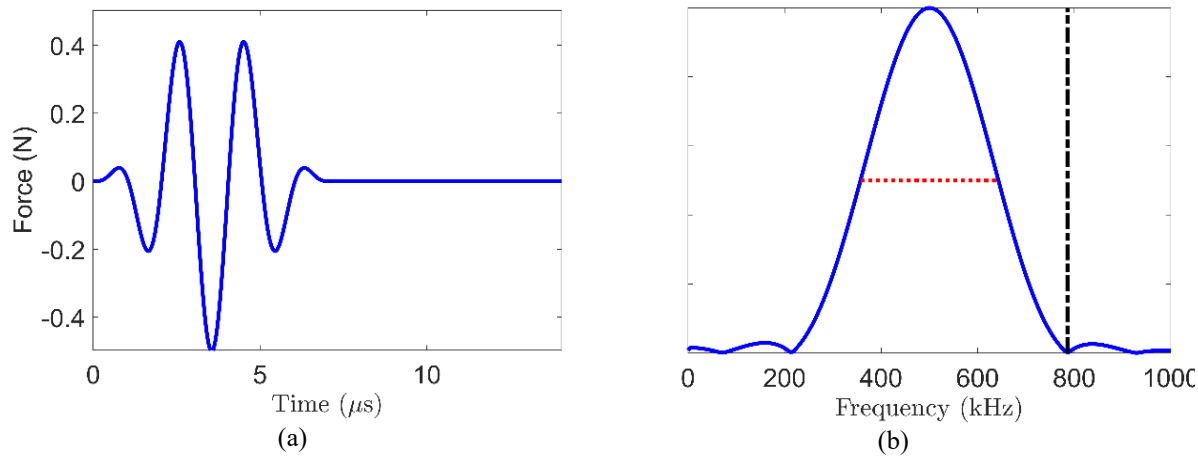

Figure 4. (a) Example of the modelled impulse force using Eq. 1, with a centre frequency of 500 kHz. (b) Fast Fourier Transform of (a) with the impulse frequency bandwidth indicated by the horizontal red dotted line, and the effective maximum frequency shown by the vertical black dashed line.

Model mesh

This section describes the mesh structure used in the model. The centre frequency of the impulse force was used to determine the mesh size for a particular model. Specifically, the maximum mesh size was 1/5th of the A0 wavelength of the chosen centre frequency [17], with the A0 wavelength for the particular centre frequencies (100, 200, and 500 kHz) determined using a commercially available database [18]. Note that the wavelength of the centre frequency was used to determine mesh size since that is the frequency that contains the bulk of the acoustic energy (i.e. Fig. 4b).
A sweeping mesh was applied to the region designated as the infinite element domain (Figs. 2a, 2b) [19]. One hundred elements in the radial direction for the infinite element domain was sufficient to minimise boundary wave reflection. A sweeping mesh of hexahedral elements was applied to the LAMDA sensor and also to the boxed region of the aluminium plate (see Fig. 2d, region 'B'), with a free triangular mesh applied to the remainder of the plate. Applying the sweeping mesh to region 'B' kept the total degrees of freedom within the range of 850k to 910k depending on the selected centre frequency.

Model solver

This section describes the conditions used in the multiphysics model solver. A time-dependent solver was used, for which both the solver time-step and maximum solve-time were adjusted based on the chosen centre frequency. Mechanical impulses with a higher centre frequency create Lamb waves that travel faster across the plate and past LAMDA sensor, and thus did not require as long a solve-time. The maximum solve time was predefined for each centre frequency, being 75, 45, and 30 µs for centre frequencies 100, 200, and 500 kHz respectively.

Regarding the time-step, the solver was set to strictly solve with a predefined time-step defined by Eq. 4. One full solve for a single modelled system (e.g. a solve with PVDF sensing elements and a centre frequency of 200 kHz) was found to take just under 2 hours using a high-end laptop PC.

$$t_s = \frac{60}{f_{max}} \tag{4}$$

Materials Research Proceedings **27** (2023) 84-94 https://doi.org/10.21741/9781644902455-11

Results and discussion

This section will present and discuss model predictions for PVDF LAMDA and RFSC LAMDA sensors, including the modelled voltage signals generated by a passing A0 wave and their relative amplitudes.

Examples of the modelled voltage waveforms generated by the PVDF LAMDA and RFSC LAMDA sensors are given in Fig. 5. In particular, Fig. 5 shows the voltage generated by element '1' (Fig. 2d) in response to the A0 Lamb wave created by a 3.5 cycle impulse at 500 kHz. The waveforms for PVDF and RFSC are alike, displaying a similar number of peaks and near-identical peak timings for the main acoustic pulse. The main difference between the waveforms is that there is significantly more voltage generated by the RFSC element compared with the PVDF element. Specifically, the positive maximum-peak ratio was RFSC/PVDF = 0.19 V/0.037 V ≈ 5.1, with a peak-to-peak ratio of RFSC/PVDF ≈ 5.4. A similar improvement is seen across the range of modelled frequencies, 100 kHz to 500 kHz. An obvious difference between the waveforms plotted in Fig. 5 is their sign. At any particular point in time the PVDF and RFSC voltage waveforms are opposite in sign due to the difference in sign between PVDF d_{31} and RFSC d_{32} (Appendix A). Another difference is the small ripple in the RFSC waveform near 22 μs, possibly due to reflections from other elements in the RFSC LAMDA array, or from the walls due to imperfect absorption at the infinite element domain boundary (Fig. 1).

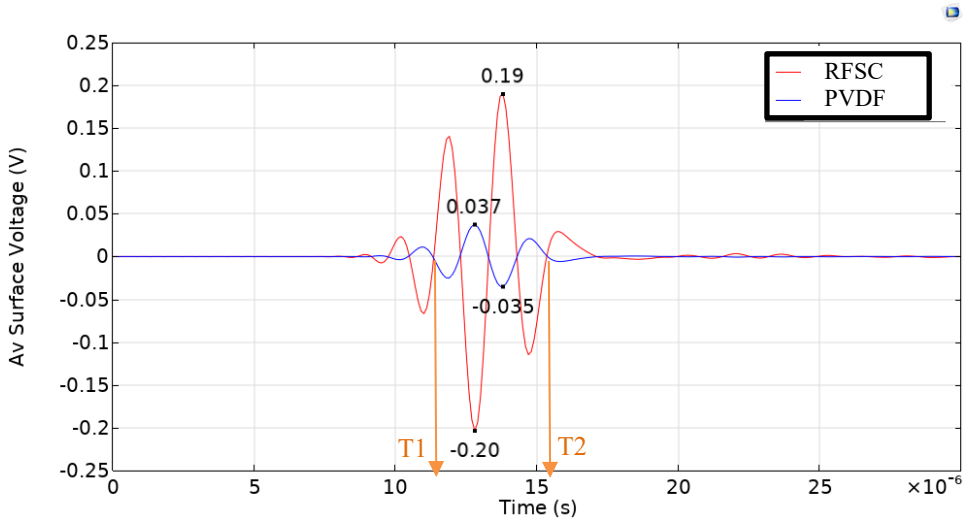

Figure 5. Model results for a 3.5 cycle impulse at 500 kHz showing average surface voltage versus time for the leftmost sensing element numbered '1' in Fig. 1d. PVDF element '1' and RFSC LAMDA element '1' are compared, and the maximum and minimum values are shown. Time 'T1' is the time taken for the main acoustic cycle to arrive at LAMDA sensor element '1', and time T2-T1 is the time length for the two main pulse cycles.

Due to the dispersive nature of Lamb wave propagation, as the centre frequency increases the group velocity of the wave increases and the pulse length decreases. Fig. 6 illustrates these effects, with the time T1 (Fig. 5) taken for the A0 pulse to travel the 30.5 mm from the plate centre to element '1' decreasing as frequency is increased. The modelled pulse duration T2-T1 decreases in a similar fashion. These modelled results indicate that the multiphysics model is behaving as expected.

Materials Research Proceedings **27** (2023) 84-94 https://doi.org/10.21741/9781644902455-11

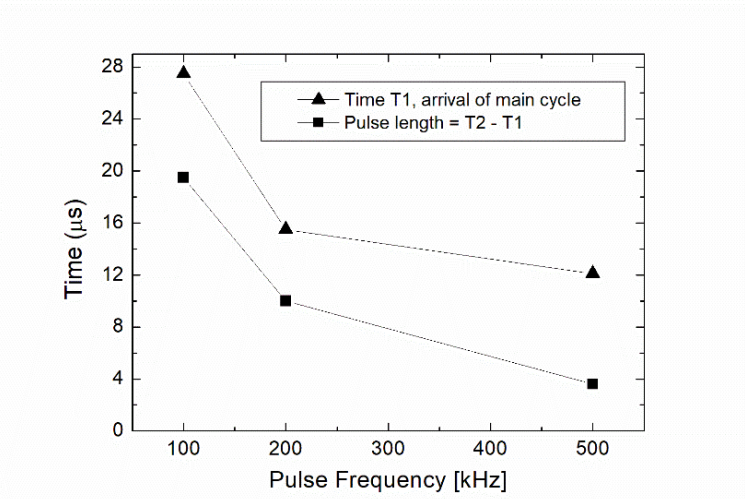

Figure 6. Model results for a 3.5 cycle impulse at different frequencies. Times T1 and T2 are defined in Fig. 5, with time 'T1' being the time taken for the main pulse cycle to arrive at LAMDA sensor element '1', and time T2-T1 is the time length for the two main pulse cycles.

Fig. 7 depicts the modelled response of the 16-element LAMDA array (Fig. 1d) for a 3.5 cycle 500 kHz impulse excitation of the plate. Fig. 7a shows the response of the elements for the PVDF LAMDA, and Fig. 7b the response of the elements for the RFSC LAMDA.

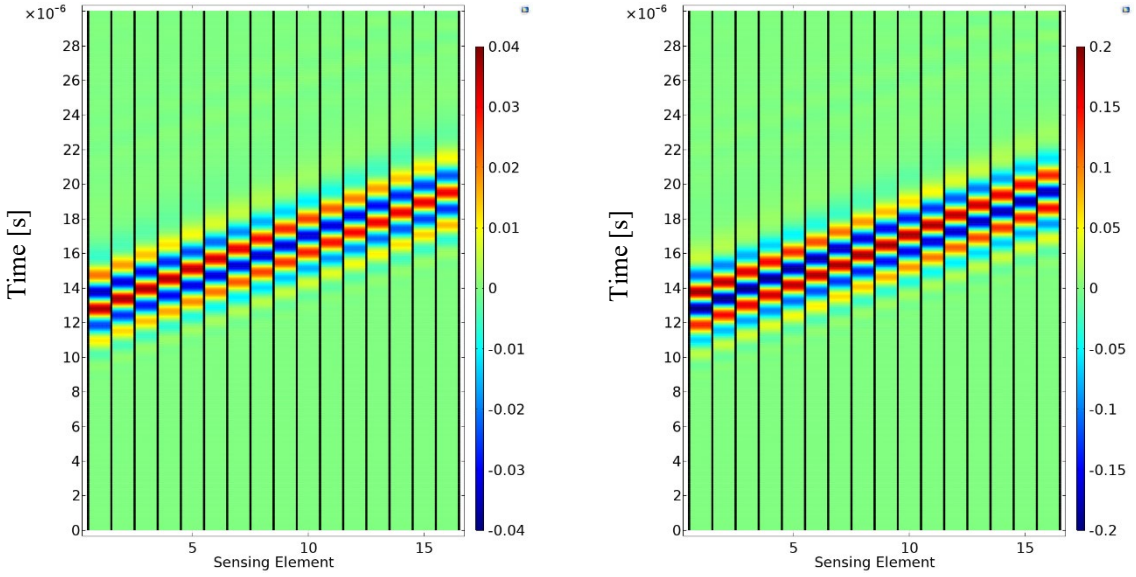

Figure 7. Model results for a 3.5 cycle 500 kHz impulse depicting the output voltage versus time for the 16 elements of the LAMDA sensing array shown in Fig. 1d, for (a) PVDF LAMDA, and (b) RFSC LAMDA.

As indicated previously, the voltages produced by RFSC LAMDA are significantly greater than those of the PVDF LAMDA (i.e. Fig. 5). Fig. 7 shows the modelled propagation of a 3.5 cycle 500 kHz A0 wave across the region containing the 16 elements that form the LAMDA sensor (i.e. region 'B' in Fig. 2c, and Fig. 2d). To aid this comparison, the scale of the colour legend for PVDF LAMDA in Fig. 7 is 5X smaller than that used for RFSC LAMDA (i.e. ±0.04 V versus ±0.2 V). Fig. 7 indicates, as expected, that the A0 pulse propagation through the Al plate and across the 16 elements is similar for PVDF LAMDA and RFSC LAMDA. The main difference is the ~5X

increase in signal voltage produced by the RFSC sensing elements. This improvement is significant, however is smaller than the signal increase that might be expected with a simple comparison of piezoelectric coefficients for RFSC and PVDF, being $d_{32} \approx -1100$ pC/N and $d_{31} \approx 13.6$ pC/N respectively.

As mentioned earlier, it is anticipated that the electromechanical coupling factor k will play an important role in determining the relative sensitivities of the two LAMDA sensor types [10]. Using parameters listed in Appendix A, the electromechanical coupling for PVDF LAMDA is $k_{31}^{PVDF} = d_{31}/\sqrt{\varepsilon_{33}^{T} * s_{11}^{E}} = 0.0845$, while for RFSC LAMDA $k_{32}^{RFSC} = d_{32}/\sqrt{\varepsilon_{33}^{T} * s_{22}^{E}} = 0.876$. The ratio of electromechanical coupling for RFSC compared with PVDF is $k_{32}^{RFSC}/k_{31}^{PVDF} = 10.4$. As mentioned, the model predicted increase in sensitivity for RFSC LAMDA was ~5X, approximately half of that expected when comparing the electromechanical coupling of RFSC and PVDF. The difference is likely due to the mechanical compliance of the aluminium plate 14.5x10^{-12} 1/Pa versus that of PVDF and that of RFSC, being 378.1x10^{-12} 1/Pa and 69.3x10^{-12} 1/Pa respectively, i.e. the mechanical strain in the PVDF elements will be dominated by the surface-strain in the aluminium plate, whereas the RFSC elements are less compliant by a factor of ~5.5 so will experience comparatively less strain. This compliance effect, and also the manufacture and characterisation of the RFSC LAMDA shown in Fig. 1b, will be reported in future work.

Conclusion

Multiphysics modelling has been performed for a Lamb wave sensor called LAMDA. The objective of the work was to investigate whether a LAMDA sensor based on relaxor ferroelectric single crystal (RFSC LAMDA) Mn-PMN-PZT will outperform the existing sensor based on polyvinylidene fluoride (PVDF LAMDA). For the purposes of modelling, both sensors were assumed to have identical geometry, with each sensor consisting of 16 piezoelectric elements and having dimensions 1 mm long, 5 mm wide, 55 μm thick, separated by 0.27 mm. For ultrasonic sensors such as LAMDA, the electromechanical coupling factor $k = d/\sqrt{\varepsilon^{T} * s^{E}}$ is considered to be an important parameter. For the two materials of interest in this work, the coupling factors are $k_{32}^{RFSC} = 0.876$ and $k_{31}^{PVDF} = 0.0845$, with the ratio between them being $k_{32}^{RFSC}/k_{31}^{PVDF} = 10.4$. This suggests that a LAMDA sensor based on RFSC could potentially be one order of magnitude more sensitive than a sensor based on PVDF. Using a normalised 3.5 cycle 500 kHz acoustic plate impulse, the multiphysics model comparison predicts that the RFSC LAMDA will produce a peak voltage response ~5X greater than the PVDF LAMDA. This is somewhat less than the factor of 10.4X suggested by the ratio of coupling factors, and is likely due to the difference in mechanical compliance between the aluminium plate and that of PVDF versus that of RFSC, i.e. the PVDF elements are 5.5X more compliant than the RFSC elements. RFSC LAMDA is currently being manufactured, the results of its experimental testing will be reported elsewhere.

Acknowledgements

The authors gratefully acknowledge the assistance of the DSTG Battle Ready Platforms program, the DSTG IEP program, and the Advanced Piezoelectric Materials and Applications Program supported by DMTC Limited (Australia) and funded by DSTG through the Next Generation Technologies Fund. The authors would also like to thank Mr. Daniel Bitton.

References

[1] N. Rajic, C. Rosalie, B. S. Vien, L.R.F. Rose, J. Smithard, W. K. Chiu, In situ wavenumber–frequency modal decomposition of acoustic emissions, Struct. Health Monitoring. 19 (2020) 2033-2050. https://doi.org/10.1177/1475921719885324

[2] C. Rosalie, N. Rajic, S. van der Velden, L.R. F. Rose, J. Smithard, W.K Chiu, Toward Composite Damage Classification Using in Situ Wavenumber-Frequency Modal Decomposition

of Acoustic Emissions, European Workshop on Structural Health Monitoring - Special Collection of 2020 Papers. 127 (2021) 647-657. https://doi.org/10.1007/978-3-030-64594-6_63

[3] X. Yao, B.S. Vien, N. Rajic, LR. F. Rose, C.H.J. Davies, W.K. Chiu, Acoustic emission of metallic specimen with surface defect during fatigue crack growth, Mater. Research Proc.. 18 (2021) 95–104. https://doi.org/10.21741/9781644901311-12

[4] N. Rajic, C. Davis, A. Thomson Acoustic-wave-mode separation using a distributed Bragg grating sensor, Smart Mater. Struct. 18 (2009) 125005. https://doi.org/10.1088/0964-1726/18/12/125005

[5] N. Rajic, C. Rosalie, C. Davis, P. Norman, A distributed sensing capability for in situ time-domain separation of Lamb waves, IEEE Eighth International Conference on Intelligent Sensors, Sensor Networks and Information Processing. (2013) 13580827. https://doi.org/10.1109/ISSNIP.2013.6529772

[6] B. Ren, CJ. Lissenden, PVDF multielement Lamb wave sensor for structural health monitoring, IEEE Trans. Ultrason Ferr. 63 (2016) 178–185. https://doi.org/10.1109/TUFFC.2015.2496423

[7] J. Smithard, N. Rajic, S. van der Velden, P. Norman, C. Rosalie, G. Steve, H. Mei, B. Lin, V. Giurgiutiu, An advanced multi-sensor acousto-ultrasonic structural health monitoring system: development and aerospace demonstration, Materials. 10 (2017) 832. https://doi.org/10.3390/ma10070832

[8] P. Kudela, M. Radzienski, W. Ostachowicz, Impact induced damage assessment by means of Lamb wave image processing, Mech. Syst. Signal Pr. 102 (2018) 23–36. https://doi.org/10.1016/j.ymssp.2017.09.020

[9] V. Giurgiutiu, Structural health monitoring: with piezoelectric wafer active sensors, Elsevier, Amsterdam, 2007. https://doi.org/10.1016/B978-012088760-6.50008-8

[10] S. Zhang, F. Li, X. Jiang, J. Kim, J. Luo, X. Geng, Advantages and challenges of relaxor-PbTiO3 ferroelectric crystals for electroacoustic transducers—a review, Prog.Mater. Sci. 68 (2015) 1–66. https://doi.org/10.1016/j.pmatsci.2014.10.002

[11] Piezoelectric parameters for PVDF, COMSOL Multiphysics materials library, 2022.

[12] B. S. Vien, S. D. Moss, W. K. Chiu, J. Thornton, C. Rosalie, N. Rajic, T. F. Doughney, and H. J. Kissick, Measured Lamb wave radiation patterns from <011> Mn-PMN-PZT relaxor ferroelectric disks on an isotropic plate, App. Phys. Lett. 113, 122902 (2018). https://doi.org/10.1063/1.5044671

[13] K. Uchino, The development of piezoelectric materials and the new perspective, in: Advanced Piezoelectric Materials Science and Technology, Woodhead Publishing Limited, Series in Electronic and Optical Materials (2010) 1-85. https://doi.org/10.1533/9781845699758.1

[14] W.P. Mason, Physical Acoustics Principles and Methods, New York: Academic. 1A (1964) 193-195.

[15] S. Ha, F-K. Chang, Adhesive interface layer effects in PZT-induced Lamb wave propagation, Smart Mater. Struct. 19 (2010) 025006. https://doi.org/10.1088/0964-1726/19/2/025006

[16] J.M. Vivar-Perez, C. Willberg, U. Gabbert, Simulation of Piezoelectric Induced Lamb Waves in Plates, Proc. Appl. Math. Mech. 9 (2009) 503 – 504. https://doi.org/10.1002/pamm.200910224

[17] COMSOL Multiphysics, Resolving time dependent waves, https://www.comsol.com/support/knowledgebase/1118 , accessed 1st September 2022.

[18] M. Lowe, Disperse: Guided wave dispersion curve calculation, http://www.disperse.software/index.html, accessed 1st September 2022.

[19] COMSOL Multiphysics, Setup and Meshing of Infinite Elements, Perfectly Matched Layers, and Absorbing Layers, https://www.comsol.com/support/knowledgebase/1272 , accessed 1st September 2022.

[18] M. Lowe. Disperse: Guided wave dispersion curve calculation. Available from http://www.disperse.software/index.html , accessed 1st September 2022.

[19] COMSOL Multiphysics, "Setup and Meshing of Infinite Elements, Perfectly Matched Layers, and Absorbing Layers," https://www.comsol.com/support/knowledgebase/1272 , accessed 1st September 2022.

Appendix A

Table A1 lists the modelled mechanical properties used for the aluminium plate shown in Fig. 2. Tables A2 and A3 list the electro-mechanical properties for the transducer materials used in the PVDV and RFSC LAMDA sensors.

Table A1. Mechanical properties for modelled aluminium plate.

Mechanical Property	**Value for Aluminium**
Density (kg/m^3)	2700
Mechanical Compliance (10^{-12} 1/Pa)	14.5
Poisson's Ratio	0.33

Table A2. Electrical and mechanical model parameters for PVDF.

Electrical		**Mechanical**	
d_{31} (pC/N)	13.58	S_{11} (10^{-12} 1/Pa)	378.1
d_{32} (pC/N)	1.476	S_{12} (10^{-12} 1/Pa)	-148.2
d_{33} (pC/N)	-33.8	S_{13} (10^{-12} 1/Pa)	-172.4
ε_{11}	7.4	S_{22} (10^{-12} 1/Pa)	378.1
ε_{22}	9.3	S_{23} (10^{-12} 1/Pa)	-172.4
ε_{33}	7.74	S_{33} (10^{-12} 1/Pa)	1092
		S_{44} (10^{-12} 1/Pa)	1110
		S_{55} (10^{-12} 1/Pa)	1110
		S_{66} (10^{-12} 1/Pa)	1428
		Density (kg/m^3)	1780

Table A3. Electrical and mechanical model parameters for the RFSC Mn-PMN-PZT.

Electrical		**Mechanical**	
d_{31} (pC/N)	405	S_{11} (10^{-12} 1/Pa)	16.2
d_{32} (pC/N)	-1100	S_{12} (10^{-12} 1/Pa)	-25.4
d_{33} (pC/N)	820	S_{13} (10^{-12} 1/Pa)	14.9
d_{24} (pC/N)	145	S_{22} (10^{-12} 1/Pa)	69.3
d_{15} (pC/N)	1997	S_{23} (10^{-12} 1/Pa)	-43.6
ε_{11}	2891	S_{33} (10^{-12} 1/Pa)	37
ε_{22}	861	S_{44} (10^{-12} 1/Pa)	19.5
ε_{33}	2570	S_{55} (10^{-12} 1/Pa)	179
		S_{66} (10^{-12} 1/Pa)	26.8
		Density (kg/m^3)	7900

Materials Research Proceedings **27** (2023) 84-94 https://doi.org/10.21741/9781644902455-11

Appendix B

The expression for a Hann-Windowed wave centred about $t = 0$ is defined by Eq. B1,

$$h(t) \triangleq A_0 \cos^2\left\{\frac{\pi t}{L}\right\} \qquad \left(|t| \leq \frac{L}{2}\right) \tag{B1}$$

where the amplitude defined by A_0 is typically $\frac{1}{L}$, with L being the window length/duration.

A translation of $\frac{\pi}{2}$ can manipulate this expression to begin at $t = 0$ and end at window length $t = L$. The resulting simplified expression is defined by Eq. B2.

$$h(t) \triangleq A_0 \ \sin^2\left\{\frac{\pi t}{L}\right\} \quad (0 \leq t \leq L) \tag{B2}$$

For a wave of C cycles, centred around a frequency f, the resulting window length L is defined by Eq. B3,

$$L = C \cdot \frac{1}{f} \tag{B3}$$

where $\frac{1}{f}$ is the period for one cycle. Substituting B3 into B2 and simplifying generates the resulting expression shown by Eq. B4,

$$h(t) \triangleq A_0 \ \sin^2\left\{\frac{\pi t f}{C}\right\} \quad (0 \leq t \leq L) \ . \tag{B4}$$

The generalized expression of a traveling wave is given by Eq. B5,

$$y = \sin\ \{2\pi f t\} \ . \tag{B5}$$

Multiplying Eq. B5 with the derived expression for the Hann-Windowed wave shown in Eq. B4 gives us the resulting expression for the impulse wave in Eq. B6,

$$y(t) = A_0 \ \sin^2\left\{\frac{\pi t f}{C}\right\} \sin\{2\pi f t\} \quad (0 \leq t \leq L) \ . \tag{B6}$$

Finally, a time delay t_0 is applied to prevent instantaneous stresses in the model that can produce solver errors, the result of which is defined by Eq. B7,

$$y(t) = A_0 \ \sin^2\left\{\frac{\pi f}{C}(t - t_0)\right\} \sin\{2\pi f(t - t_0)\} \quad (0 \leq t \leq L) \ . \tag{B7}$$